The influence of RBF differentiation on the accuracy of the alternative LBIE method for solving the Navier-Stokes equations

E. H. Ooi & V. Popov
Environmental and Fluid Mechanics, Wessex Institute of Technology, UK

Abstract

In this paper, the local boundary integral equation (LBIE) method employing the simplified approach for imposing the boundary conditions is used to solve the lid driven cavity problem described by the velocity-vorticity formulations of the Navier-Stokes equations. The objective of this study is to investigate how the differentiation of the radial basis functions carried out to approximate the spatial gradients in the simplified approach affects the accuracy of the numerical solutions in problems where knowledge of the spatial gradients is of significance. The numerical results were compared with benchmark solutions and with those obtained using the radial basis integral equation method; an integral equation based meshless method that does not involve the differentiation of the RBF to approximate the spatial gradients.

Keywords: velocity-vorticity formulation, radial basis functions, meshless methods, Navier-Stokes equations, integral equations.

1 Introduction

The local boundary integral equation (LBIE) method is a meshless method that is formulated around the integral equation and the use of a companion solution [1]. One of the difficulties when implementing the LBIE is that integration over part of the global boundary is required, which involves near-singular and singular integrals. Although global boundary integration can be avoided by imposing the boundary conditions (BCs) using collocation schemes [1], this approach is based on the strong formulation and requires a highly accurate interpolation scheme to yield accurate numerical results.

WIT Transactions on Modelling and Simulation, Vol 54, © 2013 WIT Press
www.witpress.com, ISSN 1743-355X (on-line)
doi:10.2495/BEM130031

Recently, Ooi and Popov [2] proposed a simplified method for imposing the BCs in the LBIE. This alternative LBIE method, hereafter denoted by ALBIE, maintains the weak formulation by enforcing the integral equation derived using the fundamental solution and the Green's second identity on the boundary. The subdomains for the nodes at the boundary remain circular and unknown field variables exterior to the solution domain are extrapolated using the surrounding nodes. All the integrations are performed over the circular subdomain, which avoids the near-singular and singular integrals since the source point is always at the centre of the subdomain.

Provided that third order radial basis functions (RBF) are used, the results obtained using the ALBIE were found to be comparable to those of the LBIE. Nevertheless, there are concerns that the differentiation of the RBF carried out to approximate the spatial gradients can affect the accuracy of the numerical scheme, particularly in problems where knowledge of the spatial gradients is of significance. This is investigated in the present paper, where the lid driven cavity problem is solved. The problem is described by the velocity-vorticity formulations of the Navier-Stokes equations, which present an excellent example as the accuracy of the numerical scheme depends strongly on how accurate the velocity spatial gradients are evaluated. The performance of the ALBIE is compared with the radial basis integral equation (RBIE) method; an integral equation based meshless method that does not involve the differentiation of the RBF to approximate the spatial gradients [3, 4].

This paper is organized into five sections. Section 2 describes the lid driven cavity problem and derives briefly the ALBIE. The steps involved in implementing the ALBIE to solve the lid driven cavity problem are given in Section 3. Numerical results are presented in Section 4 and conclusions are given in Section 5.

2 Mathematical formulations

2.1 The lid driven cavity problem

The velocity-vorticity formulation of the Navier-Stokes equations governing the two-dimensional incompressible flow is given in non-dimensional form by:

$$\nabla^2 u(r,t) = -\nabla \times \omega(r,t), \quad \text{for } r \in \Omega, \tag{1a}$$

$$\nabla^2 \omega(r,t) = \frac{\partial \omega(r,t)}{\partial t} + \mathrm{Re}\big(u(r,t)\nabla \omega(r,t)\big), \quad \text{for } r \in \Omega, \tag{1b}$$

where $r = (x_1,x_2)$ is the field point coordinates inside the domain Ω, $u_i = (u_1,u_2)$ is the velocity vector, ω is the vorticity, t is time and Re is the Reynolds number. Equations (1a) and (1b) represent the velocity Poisson equation and the vorticity transport equation, respectively.

Figure 1 illustrates the two-dimensional lid driven cavity problem. The lid is represented by the top boundary and moves in the x_1-direction at velocity $u_1 = 1$, while all other boundaries are stationary walls such that the stationary no slip condition can be prescribed.

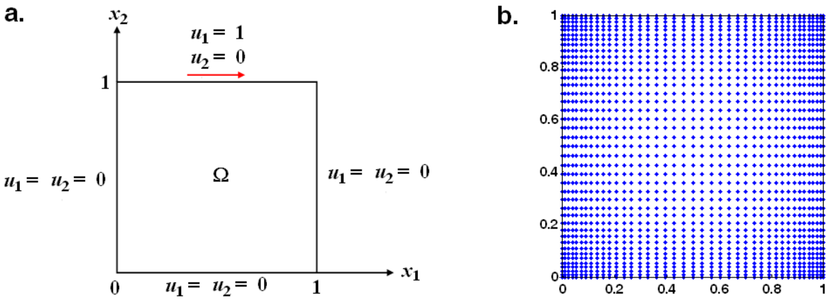

Figure 1: (a) The lid driven cavity problem and (b) the distribution of nodes based on the hyperbolic grid stretching.

2.2 The local boundary integral equation method

In this section, only a brief derivation of the LBIE is presented. Readers are referred to the paper by Ooi and Popov [2] for a more complete derivation of the LBIE and the ALBIE. To carry out the LBIE, N_t collocation nodes are distributed across $\Omega \cup \Gamma$, where Γ is the boundary of the domain Ω. A circular subdomain Ω_m enclosed by the local boundary Γ_m, centred on each node is generated. These subdomains may overlap, may be of different radius and may extend beyond the boundary of the solution domain.

Consider the following equation:

$$\nabla^2 \phi(r,t) = \frac{\partial \phi(r,t)}{\partial t} + b(r,t,\phi,\nabla\phi), \quad \text{for } r \in \Omega_m, \tag{2}$$

where ϕ and b are represented by u and $-\nabla\times\omega$ in (1a), and ω and $\mathrm{Re}(u\nabla\omega)$ in (1b). The term$\partial\ \phi/\partial t$ vanishes for the velocity Poisson equation. Following the introduction of the companion solution [1], the integral equation representation of (2) for ξ at the interior of Ω is given by:

$$\phi(\xi,t) = \int_{\Gamma_m} \phi(r,t) \frac{\partial \Phi^*(r;\xi)}{\partial n} \mathrm{d}\Gamma + \iint_{\Omega_m} \left(b + \frac{\partial \phi(r,t)}{\partial t} \right) \Phi^*(r;\xi) \mathrm{d}\Omega, \tag{3}$$

where $\xi = (\xi_1, \xi_2)$ is the source point coordinate and $\Phi^*(r;\xi)$ is the modified test function given by:

$$\Phi^*(r;\xi) = \frac{1}{2\pi} \log[\Re(r;\xi)/R_m], \tag{4}$$

where $\Re$ is the Euclidean distance between the field point and the source point and R_m is the radius of the subdomain Ω_m.

Equation (3) is used in both the LBIE and the ALBIE when the source point ξ is at the interior of Ω. For ξ at the boundary, the ALBIE employs the following equation [2]:

$$\frac{\partial\phi(\xi,t)}{\partial\xi_i}=\int_{\Gamma_m}\left[\phi(r,t)\frac{\partial^2\Phi(r;\xi)}{\partial\xi_i\partial n}-n_j\frac{\partial\phi(r,t)}{\partial x_j}\frac{\partial\Phi(r;\xi)}{\partial\xi_i}\right]\mathrm{d}\Gamma$$
$$+\iint_{\Omega_m}\left(b+\frac{\partial\phi(r,t)}{\partial t}\right)\frac{\partial\Phi(r;\xi)}{\partial\xi_i}\mathrm{d}\Omega, \tag{5}$$

where $\Phi(r;\xi)$ is the fundamental solution of the Laplace equation.

The field variables ϕ, b and $\partial\phi/\partial t$ in (3) and (5) can be approximated in terms of their values at the surrounding nodes by using the RBF interpolations, i.e.:

$$\phi(r,t)\approx\sum_{k=1}^{N_a}f(r;r^{(k)})\alpha^{(k)},\quad b+\frac{\partial\phi(r,t)}{\partial t}\approx\sum_{k=1}^{N_a}f(r;r^{(k)})\alpha^{(k)}, \tag{6}$$

where N_a is the number of points used in the interpolation, f is the RBF and α are unknown coefficients that can be determined by collocating (5) at all the N_a points. This sets up a system of linear algebraic equations that can be inverted yielding:

$$\phi(r,t)\approx\sum_{n=1}^{N_a}\phi^{(n)}\sum_{k=1}^{N_a}W^{(kn)}f(r;r^{(k)}),\quad b\approx\sum_{n=1}^{N_a}\left(b^{(n)}+\frac{\partial\phi^{(n)}}{\partial t}\right)\sum_{k=1}^{N_a}W^{(kn)}f(r;r^{(k)}), \tag{7}$$

where $W^{(kn)}$ are the coefficients of the inverse matrix obtained from the RBF interpolations and $\phi^{(n)}$ and $b^{(n)}$ are values of ϕ and b at the n^{th} interpolation point. The unknown spatial gradients$\partial\ \phi/\partial x_j$ in (5) can be expressed in terms of $\phi^{(n)}$ by differentiating the first expression in (7). This leads to:

$$\frac{\partial\phi(r,t)}{\partial x_j}\approx\sum_{n=1}^{N_a}\phi^{(n)}\sum_{k=1}^{N_a}W^{(kn)}\frac{\partial f(r;r^{(k)})}{\partial x_j}, \tag{8}$$

As in the RBIE [3, 4], the interpolations in (7) and (8) remain valid for part of the subdomain that is exterior to the solution domain. In this case, the unknowns are extrapolated by the surrounding nodes.

Substituting (6), (7) and (8) into (3) and (5) yields:

$$\phi(\xi,t)=\mathbf{F}_0\{\phi(t)\}+\Psi\{\mathbf{b}+\frac{\partial\phi(t)}{\partial t}\},\ \text{for } \xi \text{ at the interior,} \tag{9a}$$

$$\frac{\partial\phi(\xi,t)}{\partial\xi_i}=\mathbf{H}_0\{\phi(t)\}-\sum_j\mathbf{H}_{1j}\{\phi(t)\}+\Pi\{\mathbf{b}+\frac{\partial\phi(t)}{\partial t}\},\ \text{for } \xi \text{ at the boundary,} \tag{9b}$$

where

$$
\begin{aligned}
&\mathbf{F}_0=\sum_{k=1}^{N_a}W_{kn}\int_{\Gamma_s}f(r;r^{(k)})\frac{\partial\Phi^*}{\partial n}\mathrm{d}\Gamma,\quad \Psi=\sum_{k=1}^{N_a}W_{kn}\iint_{\Omega_m}f(r;r^{(k)})\Phi^*\mathrm{d}\Omega,\\
&\mathbf{H}_0=\sum_{k=1}^{N_a}W_{kn}\int_{G_s}f(r;r^{(k)})\frac{\partial^2\Phi^*}{\partial\xi_i\partial n}\mathrm{d}\Gamma,\ \mathbf{H}_{1j}=\sum_{k=1}^{N_a}W_{kn}\int_{G_s}n_j\frac{\partial f(r;r^{(k)})}{\partial x_j}\frac{\partial\Phi}{\partial\xi_i}\mathrm{d}\Gamma,\\
&\Pi_i=\sum_{k=1}^{N_a}W_{kn}\iint_{\Omega_m}f(r;r^{(k)})\frac{\partial\Phi}{\partial\xi_i}\mathrm{d}\Omega,\qquad\qquad \text{for } k=1,2,\ldots,N_a,
\end{aligned}
\tag{10}
$$

The boundary and domain integrals in (10) can be evaluated numerically using formulae such as the Gaussian quadrature.

2.3 The time stepping scheme

The time-dependent variables in (9a) and (9b) are dealt with by using the time-stepping scheme [5]:

$$
\begin{aligned}
&\phi(r,t)\approx\frac{1}{2}[\phi(r,t+\tfrac{1}{2}\Delta t)+\phi(r,t-\tfrac{1}{2}\Delta t)],\\
&\frac{\partial\phi(r,t)}{\partial x_j}\approx\frac{1}{2}\left(\frac{\partial\phi(r,t+\frac{1}{2}\Delta t)}{\partial x_j}+\frac{\partial\phi(r,t-\frac{1}{2}\Delta t)}{\partial x_j}\right),\\
&\frac{\partial\phi(r,t)}{\partial t}\approx\frac{1}{\Delta t}[\phi(r,t+\tfrac{1}{2}\Delta t)-\phi(r,t-\tfrac{1}{2}\Delta t)],
\end{aligned}
\tag{11}
$$

where Δt is the time step. Substituting (11) into (9a) and (9b) yields:

$$
\frac{1}{2}[\phi^+(\xi)+\phi^-(\xi)]=\frac{1}{2}\mathbf{F}_0\{\phi^++\phi^-\}+\Psi\{\mathbf{b}+\frac{\phi^+(\xi)-\phi^-(\xi)}{\Delta t}\},
\tag{12a}
$$

$$
\begin{aligned}
\frac{1}{2}[\frac{\partial\phi^+}{\partial\xi_i}+\frac{\partial\phi^-}{\partial\xi_i}]&=\frac{1}{2}\mathbf{H}_0\{\phi^++\phi^-\}-\frac{1}{2}\sum_j\mathbf{H}_{1j}\{\frac{\partial\phi^+}{\partial x_j}+\frac{\partial\phi^-}{\partial x_j}\}\\
&+\Pi\{\mathbf{b}+\frac{\phi^+(\xi)-\phi^-(\xi)}{\Delta t}\},
\end{aligned}
\tag{12b}
$$

where the superscripts '+' and '–' indicates values of variables at time levels $t+\Delta t/2$ and $t-\Delta t/2$, respectively. Note that the approximations in (11) are used inside term **b** in (12a) and (12b) in the case when b contains $\phi(r,t)$ and $\partial\phi(r,t)/\partial x_j$.

3 Numerical implementation

3.1 Collocation procedure

For a numerical procedure, the node ξ is collocated at the N_t nodes. When ξ is at the interior, (12a) is used to set up the system of equations. When ξ is at the boundary where the Dirichlet condition is prescribed, no equation is enforced since the values of the potential variables are known. Since the lid driven cavity problem does not involve the Neumann condition (see Figure 1), (12b) is not used to set up the system of equations. Instead, (12b) is used to determine the values of the spatial gradients during post-processing.

3.2 Time-stepping

If the values of ϕ^- and $\partial\phi^-/\partial x_j$ are known at each time step, then (12a) and (12b) along with the prescribed initial-boundary conditions give rise to a system of linear algebraic equations that can be solved for the unknowns ϕ^+ and $\partial\phi^+/\partial x_j$ on the boundary and interior of the solution domain. If $t = \Delta t/2$, then the values of $\phi_n(0)$ and∂ $\phi(0)/\partial x_j$ are given by the prescribed initial conditions. Unknown values $\phi(\Delta t)$ and ∂ $\phi(\Delta t)/\partial x_j$ on the boundary and interior of the solution domain can be obtained by solving the system of linear algebraic equations assembled from (12a) and (12b). With $\phi(\Delta t)$ and ∂ $\phi(\Delta t)/\partial x_j$ known, values of $\phi(3\Delta t/2)$ and $\partial\phi(3\Delta t/2)/\partial x_j$ can be calculated. This procedure may be repeated to obtain values of the field functions and its gradients at higher time levels until the desired time level is reached.

3.3 Iterative scheme

An important step when solving the velocity-vorticity formulations of the Navier-Stokes equations is the calculations of the boundary vorticity to be used as boundary conditions when solving the vorticity transport equation. The boundary vorticity can be calculated by using the definition of vorticity:

$$\omega = \frac{\partial u_2}{\partial x_1} - \frac{\partial u_1}{\partial x_2}, \tag{13}$$

where the gradients of u are obtained from the solutions of the velocity Poisson equation. To couple the velocity and the vorticity fields, an iterative procedure that solves sequentially for the velocities in the x_1- and x_2-directions and the vorticity is developed. This scheme is similar to that reported in [6] and shall not be repeated here.

4 Numerical results

All the numerical simulations were carried out using the third order polyharmonic spline of the form [2]:

$$f(r;r^{(k)}) = \Re^6(r;r^{(k)})\log(\Re(r;r^{(k)})). \tag{14}$$

The RBF in (14) is augmented with a third order global polynomial $p(r)$, given by:

$$\begin{aligned} p(r) = a_0 + a_1x_1 + a_2x_2 + a_3x_1^2 + a_4x_1x_2 + a_5x_2^2 + a_6x_1^3 \\ + a_7x_1^2x_2 + a_8x_1x_2^2 + a_9x_2^3. \end{aligned} \tag{15}$$

A total of $N_a = 25$ points were chosen for the RBF interpolations.

The radii of the subdomains at the interior were chosen to be the distance to the nearest node, while the radii of the subdomains at the boundary were chosen to be 0.1 times the distance to the nearest node. This ensures that errors due to the extrapolation of the field variables are minimized. All the boundary and domain integrals were evaluated numerically using the Gaussian quadrature with 20 and 400 (20×20) points, respectively.

In the present study, non-uniform nodes distributions were chosen to carry out the numerical simulations. Higher density of nodes was placed near the corners and the boundaries of the cavity. This is achieved based on the hyperbolic grid stretching:

$$x_j^{(m)} = \frac{1-\tanh(\varepsilon(1-m/m_{\max}))}{\tanh(\varepsilon)}, \qquad (16)$$

where $x_j^{(m)}$ is the m^{th} node in the j-direction and ε is a constant that controls the degree of stretching of the computational grid. In this study, ε was chosen to be 1.15. Figure 1(b) shows the distribution of a 51 × 51 grid generated using the hyperbolic grid stretching method. Three cases of Re were investigated, i.e. Re = 100, 400 and 1000. A total of N_t = 1681 and 3721 nodes were used to solve the flow at Re = 100 and 400, respectively. For the flow at Re = 1000, simulations were carried out for N_t = 6561, 10201 and 14641 nodes to examine the accuracy of the numerical scheme. All computations were carried out in an Intel Xeon 3.0GHz workstation with 20GB of RAM.

Table 1 shows the minimum velocity in the x_1-direction and the maximum and minimum velocity in the x_2-direction. The numerical results obtained using

Table 1: Maximum and minimum values of u_1 and u_2 for flows at Re = 100, 400 and 1000.

	min(u_1)	min(u_2)	max(u_2)
Re = 100			
ALBIE (41×41)	-0.2232	-0.2536	0.1809
RBIE (41×41)	-0.2184	-0.2529	0.1884
Benchmark*	-0.2109	-0.2453	0.1753
Re = 400			
ALBIE (61×61)	-0.3139	-0.4307	0.2916
RBIE (61×61)	-0.3405	-0.4602	0.3150
Benchmark*	-0.3273	-0.4499	0.3020
Re = 1000			
ALBIE (81×81)	-0.3195	-0.4547	0.3203
ALBIE (101×101)	-0.3537	-0.4910	0.3363
ALBIE (121×121)	-0.3489	-0.4794	0.3380
RBIE (121×121)	-0.3807	-0.4974	0.3638
Benchmark*	-0.3829	-0.5155	0.3710

*Ghia *et al.* [7] using 129 × 129 grid.

the RBIE with the third order RBF (see (14) and (15)) and the benchmark solutions of Ghia *et al.* [7] are also shown for comparisons. It is clear that the ALBIE produced results that were comparable and in some cases, more accurate than the RBIE for flows at Re = 100 and 400. As Re increased to 1000, the solutions of the ALBIE deviated slightly from the benchmark solutions. On the other hand, the solutions of the RBIE were considerably more accurate than the ALBIE when compared with the benchmark solutions.

Figure 2 plots the velocity in the x_1- and x_2-directions along the geometric centre of the cavity, respectively, for flows at Re = 100, 400 and 1000. For Re = 100 and 400, the numerical results obtained using the ALBIE were comparable to that of the RBIE and the benchmark solutions. For Re = 1000, it appears that the numerical solutions of the ALBIE were less accurate than the RBIE when compared to the benchmark solutions. The lower accuracy is due to the lower order RBF used to approximate the spatial gradients. The differentiation of the RBF in (8) means that the spatial gradients are approximated using a second order interpolation function instead of one that is third order, as in the RBIE.

Table 2 summarizes the computational parameters of the ALBIE and the RBIE. The pre-processing time refers to the time used to evaluate the boundary and domain integrals. One may observe that the ALBIE generates less number of equations than the RBIE; the larger number of equations of the RBIE is due to the introduction of two additional equations to each node to account for the spatial gradients [3, 4]. The larger number of equations naturally led to a longer mean CPU time per iteration. In this case, the mean CPU time per iteration of the RBIE was more than five times that of the ALBIE. The pre-processing time of the ALBIE was approximately twice longer than that needed by the RBIE and this was primarily due to the additional evaluations of the integrals $\mathbf{H}_{1,j}$ in (10), which was not evaluated in the RBIE.

Table 2: Computational parameters of the ALBIE and the RBIE.

	No. of nodes (N_t)		
	1681	3721	6561
ALBIE			
No. of equations	1521	3481	6241
Pre-processing (s)	12.34	25.88	48.77
Mean time per iteration (s)	0.37	0.94	2.03
RBIE			
No. of equations	4883	10923	19363
Pre-processing (s)	5.63	12.78	23.39
Mean time per iteration (s)	1.85	5.29	12.38

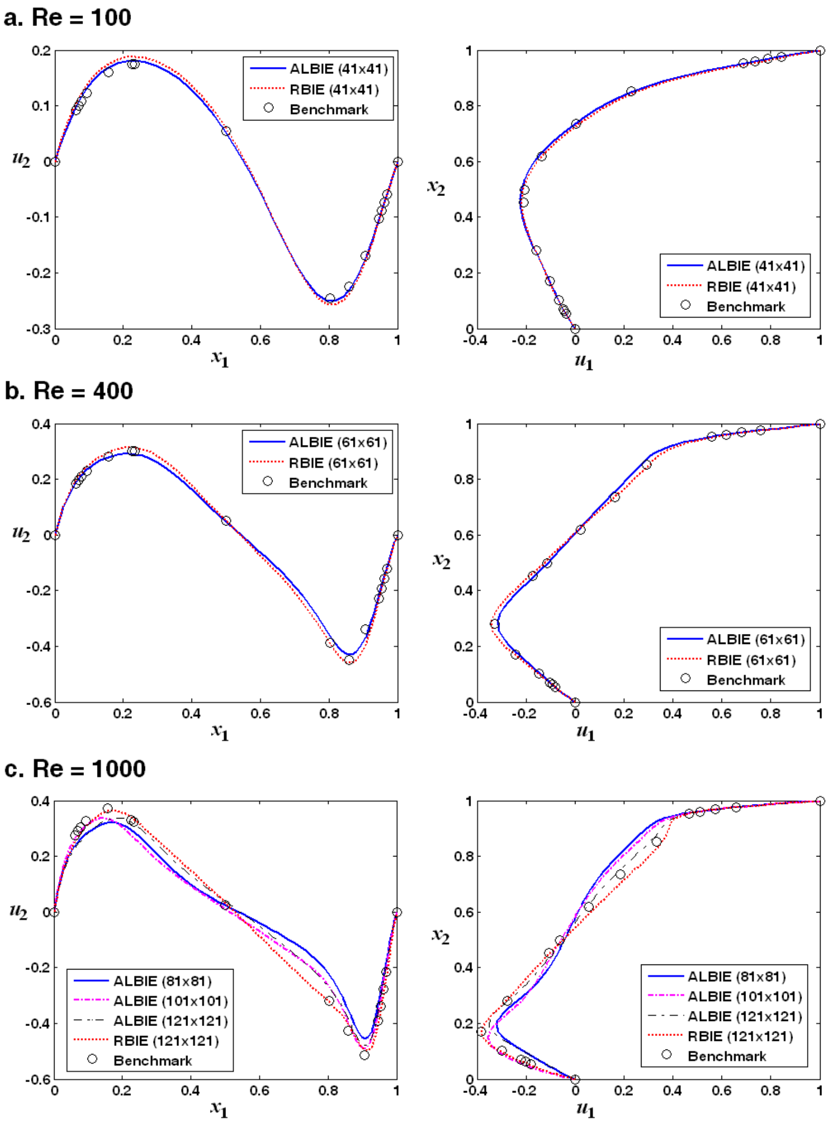

a. Re = 100

b. Re = 400

c. Re = 1000

Figure 2: Plots of u_1 and u_2 along the geometric centre of the cavity for (a) Re = 100, (b) Re = 400 and (c) Re = 1000.

5 Conclusions

In this paper, the effects of differentiating the RBFs to approximate the spatial gradients in the ALBIE have been investigated by solving the lid driven cavity problem described by the velocity-vorticity formulation of the Navier-Stokes equations. This example was chosen as the accuracy of the numerical solutions depends strongly on how accurate the vorticity is evaluated from the velocity spatial gradients (see (13)).

While flows at Re = 100 and 400 can be solved accurately with the ALBIE, the numerical solutions obtained for the flow at Re = 1000 were still far from satisfactory. Given the considerably shorter CPU time, there are clearly some advantages of using the ALBIE over the RBIE. To make the ALBIE more applicable to a wide range of problems, it is important that its accuracy for solving problems with large degrees of nonlinearity is significantly improved.

References

[1] Zhu T., Zhang J.D., Atluri S.N., A local boundary integral equation (LBIE) method in computational mechanics, and a meshless discretization approach, *Computational Mechanics*, 1998, 21: 223–235.

[2] Ooi E.H., Popov V., A simplified approach for imposing the boundary conditions in the local boundary integral equation method. *Computational Mechanics*, 2013, 57: 717−729.

[3] Popov V., Bui T.T., A meshless solution of two-dimensional convection diffusion problem. *Engineering Analysis with Boundary Elements*, 2009, 34: 680–689.

[4] Ooi E.H., Popov V., An efficient implementation of the radial basis integral equation method. *Engineering Analysis with Boundary Elements*, 2012, 36:716–726.

[5] Ang W.T., *A beginner's course in boundary element methods*, 2007, Universal Publishers, Boca Raton, Florida.

[6] Ooi E.H., Popov V., Meshless solution of 2D and 3D Stokes flow using the radial basis integral equation method. *Boundary Elements and other Mesh Reduction Methods XXXIV 2012*, WIT Transactions on Modelling and Simulation, vol. 53, pp. 73–81, Split, Croatia.

[7] Ghia U., Ghia K.N., Shin C.T., High-Re solutions for incompressible flow using the Navier-Stokes equations and a multigrid method. *Journal of Computational Physics*, 1982, 48: 387–411.